Taylor & Francis
Taylor & Francis Group

APPLICATION OF GALERKIN METHOD TO CONJUGATE HEAT TRANSFER CALCULATION

Andrej Horvat

*Reactor Engineering Division, ''Jožef Stefan'' Institute,
Ljubljana, Slovenia*

Ivan Catton

*The Henry Samueli School of Engineering and Applied Science,
Mechanical and Aerospace Engineering Department,
University of California, Los Angeles,
California, USA*

A fast-running computational algorithm based on the volume averaging technique (VAT) is developed and solutions are obtained using the Galerkin method (GM). The goal is to extend applicability of the GM to the area of heat exchangers in order to provide a reliable benchmark for numerical calculations of conjugate heat transfer problems. Using the VAT, the computational algorithm is fast-running, but still able to present a detailed picture of temperature fields in air flow as well as in the solid structure of the heat sink. The calculated whole-section drag coefficient C_d and Nusselt number Nu were compared with finite-volume method (FVM) results and with experimental data to verify the computational model. The comparison shows good agreement. The present results demonstrate that the selected Galerkin approach is capable to perform heat exchanger calculations where the thermal conductivity of the solid structure has to be taken into account.

1. INTRODUCTION

Cross-flow through the solid structure is found in a number of different applications, especially in heat exchanging devices. Although the problem has been widely studied, there are still unresolved issues, which deserve researchers' attention.

The widespread use of heat exchangers in many industrial sectors caused their development to take place in a number of rather unrelated areas. Furthermore, design solutions were based solely on experimental work because of the absence of today's powerful computers and lack of suitable numerical methods (Antonopoulos [1],

NOMENCLATURE

A_c	flow contact area of the test section	Pr	Prandtl number
A_g	heat sink ground area	Q	heat flow
A_o	interface area	Re_h	Reynolds number $=(ud_h/v_f)$
A_1	$=-M_4/\{M_3[1+\exp(\gamma)]\}$	Re_s	pore Reynolds number $=(Ud_h/v_f)$
A_2	$=-A_1-M_4/M_3$	S	specific surface $=(A_o/V)$
$A_\perp$	channel flow area	S_1	$=\alpha_s\,(d_h^2/H^2)$
c	specific heat	S_2	$=\text{Nu}_s(\lambda_f/\lambda_s)(d_hS)$
C_d	whole-section drag coefficient	T	temperature
C_l	local drag coefficient	T_g	temperature at bottom, $z=0$ position
d	pin-fin diameter	T_{in}	temperature at inflow, $x=0$ position
d_h	hydraulic diameter $=(4V_f/A_o)$	u	velocity in streamwise direction
D_1	$=uF_1$	U	velocity scale
D_2	$=F_4S_1/S_2$	v	velocity vector
D_3	$=F_5S_1/S_2+F_4$	V	representative elementary volume
D_4	$=uF_1S_1/S_2$	W	mechanical work
F_1	$=\alpha_f\,\text{Pr}\,\text{Re}_s(d_h/L)$	x	general spatial coordinate, streamwise
F_4	$=\alpha_f(d_h^2/H^2)$		coordinate
F_5	$=\text{Nu}_s(d_hS)$	z	vertical spanwise coordinate
FVM	finite-volume method	α	volume fraction
GM	Galerkin method	λ	thermal conductivity
h	arbitrary function, heat transfer coefficient	Λ	area of integration
		μ	dynamic viscosity
H	height	ν	kinematic viscosity
K	linearized drag coefficient $=(M_3u)$	ρ	density
M_2	$=\alpha_f/\text{Re}_s(d_h^2/H^2)$		
M_3	$=1/2C_l(d_hS)$	**Subscript/Superscript**	
M_4	$=d_h/L$	f	fluid phase
L	length of the test section	s	solid phase
Nu	whole-section Nusselt number		
Nu_s	pore Nusselt number $(=hd_h/\lambda_f)$		
p	pressure	**Symbols**	
Δp	whole-section pressure drop	$^-$	phase average variables
p_x	pitch between pin-fins in x direction	$^\wedge$	dimensional variables
p_y	pitch between pin-fins in y direction	$[\,]$	whole-section average variables

Barsamian and Hassan [2]). The nature of experimental work limited researchers to study only a few heat exchanger geometries and a few variations in their geometry parameters. Furthermore, the flow conditions were often limited by available experimental setups. These disadvantages, compared to numerical modeling, did not allow researchers to explore a wide range of parameters in order to find an optimal geometry. Rather, they limited the engineer's choices to well-tested and proven designs.

On the other hand, direct numerical simulation of transport phenomena in each material phase (or component) is theoretically possible, but it demands enormous computational resources even for simple geometries. This is the reason why direct approaches are rarely seen in practical engineering applications. In order to resolve most of the flow features and at the same time keep the model simple enough to serve as an engineering tool, an averaging of fluid and heat flow variables has to be performed. Recently, a unified approach based on the volume averaging technique

(VAT) has been developed and utilized for calculations of heat exchangers with isothermal (Horvat and Catton [3]) and heat conducting structures (Horvat et al. [4]).

In applying the VAT to a system of equations, transport processes in a heat exchanger are modeled as porous media flow. This generalization allows us to unify the heat transfer calculation techniques for different kinds of heat exchangers and their structures. The case-specific geometric arrangements, material properties, and fluid flow conditions enter the computational algorithm only as precalculated coefficients, which require additional modeling. This clear separation between the model and the case-specific coefficients simplifies the computational algorithm. Therefore, the algorithm is fast-running, but still able to present a detailed picture of temperature fields in air flow as well as in a solid structure of a heat sink.

In the present article, the VAT is used to model heat transfer processes in an electronic device heat sink. The geometry and boundary conditions closely follow the heat sink configuration studied experimentally in the Morrin-Martinelli-Gier Memorial Heat Transfer Laboratory at the University of California, Los Angeles. The system of porous media flow equations is solved semianalytically using the Galerkin method (GM). To demonstrate the capability and accuracy of the selected method, the results are compared with experimental data as well as with other numerical results obtained with the finite–volume method (FVM). Despite simplifications, which are needed to solve the problem semianalytically, the comparison shows good agreement.

In the past, the Galerkin solution technique was widely used for transport phenomena-related problems (Catton [5] and [6], McDonough and Catton [7], Howle [8]). It should be mentioned that the Galerkin approach is not the optimal method for this kind of calculation, due to serious limitations in the method applicability to more realistic geometries and boundary conditions. Nevertheless, the case presented here is an important benchmark on which other numerical results can be tested.

2. GOVERNING EQUATIONS FOR UNIFORM FLOW THROUGH HEAT SINK

The VAT was initially proposed in the 1960 s by Anderson and Jackson [9], Slattery [10], Marle [11], Whitaker [12], and Zolotarev and Redushkevich [13]. As the main intention of this article is to present the Galerkin solution procedure for the heat sink cross-flow, detailed description of the VAT will be omitted. Many of the important details and examples of applications can be also found in Dullien [14], Kheifets and Neimark [15], Adler [16], and Horvat [17].

To describe fluid and heat flow in an electronic device heat sink, momentum and energy transport equations for fluid flow, as well as an additional energy equations for the solid structure are needed. Applying the VAT, the transport equations are averaged over a representative elementary volume (REV), which produces porous media flow equations.

2.1. Momentum Transport

The derivation of the momentum transport equation for porous media flow starts from the momentum equation for steady-state incompressible flow, where the

effect of gravity is neglected. For uniform porous media (α_f is a constant), the momentum equation can be written as

$$\alpha_f\rho_f\bar{v}_j\frac{\partial \bar{v}_i}{\partial x_j} = -\alpha_f\frac{\partial \bar{p}_f}{\partial x_i} + \alpha_f\mu_f\frac{\partial^2 \bar{v}_i}{\partial x_j^2} - \frac{1}{V}\int\limits_{A_o} pd\Lambda_i + \frac{\mu_f}{V}\int\limits_{A_o}\frac{\partial v_i}{\partial x_j}d\Lambda_j \quad (1)$$

The integrals in Eq. (1) are a consequence of the volumetric averaging. They capture the momentum transport on the fluid–solid interface. Similar to turbulent flow, a separate model in the form of a closure relation is needed. In the present case, the integrals are replaced with the following empirical drag relation:

$$\frac{1}{2}C_l\rho_f\bar{v}_i^2 A_o = -\int\limits_{A_o} pd\Lambda_i + \mu_f\int\limits_{A_o}\frac{\partial v_i}{\partial x_j}d\Lambda_j \quad (2)$$

where C_l is the local value of the drag coefficient, which depends on the local Reynolds number. Reliable empirical data for the local drag coefficient C_l were found in Launder and Massey [18] and in Kays and London [19].

Inserting the empirical correlation (2) into Eq. (1), the momentum equation for porous media flow is given as

$$\alpha_f\rho_f\bar{v}_j\frac{\partial \bar{v}_i}{\partial x_j} = -\alpha_f\frac{\partial \bar{p}_f}{\partial x_i} + \alpha_f\mu_f\frac{\partial^2 \bar{v}_i}{\partial x_j^2} + \frac{1}{2}C_l\rho_f\bar{v}_i^2 S \quad (3)$$

It is additionally assumed that the volume average velocity through the heat sink is unidirectional $v = \{u,0,0\}$, and changes only in the vertical direction. This means that the pressure force across the entire simulation domain is balanced with shear forces. Therefore, the momentum transport equation is reduced to

$$-\alpha_f\mu_f\frac{\partial^2 \bar{u}}{\partial z^2} + \frac{1}{2}C_l\rho_f\bar{u}^2 S = \frac{\Delta p}{L} \quad (4)$$

2.2. Energy Transport in Fluid

The energy transport equation for fluid flow is developed from the energy transport equation for steady-state incompressible flow. For uniform porous media it is written as

$$\alpha_f\rho_f c_f\bar{v}_j\frac{\partial \bar{T}_f}{\partial x_j} = \alpha_f\lambda_f\frac{\partial^2 \bar{T}_f}{\partial x_j^2} + \frac{\lambda_f}{V}\int\limits_{A_o}\frac{\partial T}{\partial x_j}d\Lambda_j \quad (5)$$

The integral in Eq. (5) represents the interphase heat exchange between fluid flow and the solid structure, and it requires additional modeling. In the present case an empirical linear relation between the fluid and the solid temperature is taken as an appropriate model for the interphase heat flow:

$$h(\bar{T}_f - \bar{T}_s)A_o = -\lambda_f\int\limits_{A_o}\frac{\partial T}{\partial x_j}d\Lambda_j \quad (6)$$

where h is the local value of the heat transfer coefficient, which depends on the local Reynolds number. The data for the local heat transfer coefficient h were taken from Žukauskas and Ulinskas [20] for low Reynolds numbers, whereas for higher Reynolds numbers, the experimental data from Kays and London [19] were more appropriate.

Inserting the relation (6) into Eq. (5) the energy transport equation for fluid flow can be written as

$$\alpha_f \rho_f c_f \bar{v}_j \frac{\partial \bar{T}_f}{\partial x_j} = \alpha_f \lambda_f \frac{\partial^2 \bar{T}_f}{\partial x_j^2} - h(\bar{T}_f - \bar{T}_s)S \tag{7}$$

The energy transport equation for fluid flow (7) is further simplified with the velocity unidirectional assumption. Therefore, the temperature field in the fluid is formed as a balance between thermal convection in the streamwise direction, thermal diffusion, and the heat, which is transferred from the solid structure to fluid flow. Thus, the differential form of the energy equation for the fluid is

$$\alpha_f \rho_f c_f \bar{u} \frac{\partial \bar{T}_f}{\partial x} = \alpha_f \lambda_f \frac{\partial^2 \bar{T}_f}{\partial z^2} - h(\bar{T}_f - \bar{T}_s)S \tag{8}$$

2.3. Energy Transport in Solid

In a solid phase, thermal diffusion is the only mechanism of heat transport. Therefore, the energy transport equation for the solid structure is reduced to the simple diffusion equation

$$0 = \alpha_s \lambda_s \frac{\partial^2 \bar{T}_s}{\partial x_j^2} + \frac{\lambda_s}{V} \int_{A_o} \frac{\partial T}{\partial x_j} d\Lambda_j \tag{9}$$

where the integral captures the interphase heat exchange. Closure is obtained by substituting the linear relation

$$h(\bar{T}_f - \bar{T}_s)A_o = \lambda_s \int_{A_o} \frac{\partial T}{\partial x_j} d\Lambda_j \tag{10}$$

in Eq. (9). The VAT energy transport equation for the solid structure is now written as

$$0 = \alpha_s \lambda_s \frac{\partial^2 \bar{T}_s}{\partial x_j^2} + h(\bar{T}_f - \bar{T}_s)S \tag{11}$$

The heat sink structure in each REV is only loosely connected in horizontal directions (see Figure 1). As a consequence, only the thermal diffusion in the vertical direction is in balance with the heat leaving the structure through the fluid–solid interface, whereas the thermal diffusion in the horizontal directions can be neglected. This simplifies the energy equation for the solid structure to

$$0 = \alpha_s \lambda_s \frac{\partial^2 \bar{T}_s}{\partial z^2} + h(\bar{T}_f - \bar{T}_s)S \tag{12}$$
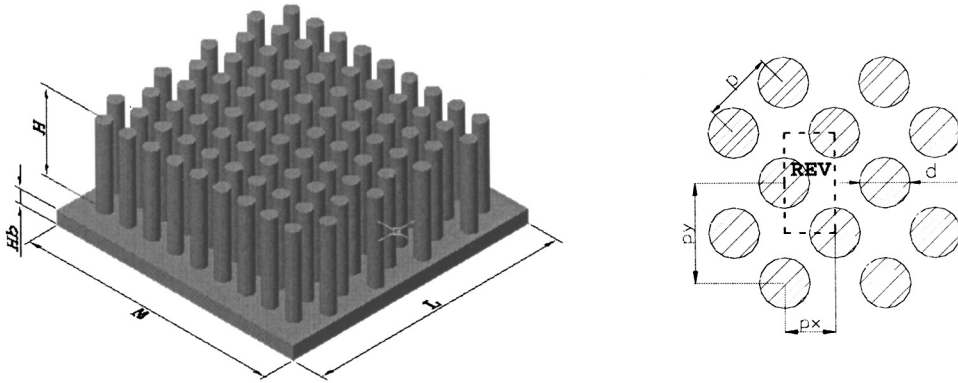
Figure 1. Experimental test section with the pin-fins arrangement.

3.   SIMULATION SETUP

The results from numerical simulations are compared with the experimental data taken in the Morrin-Martinelli-Gier Memorial Heat Transfer Laboratory at the University of California, Los Angeles. Therefore, the geometry of the simulation domain follows the geometry of the experimental test section, where the experimental data described by Rizzi et al. [21] were obtained.

3.1.   Geometry

The general arrangement of the heat sink pin-fins is given in Figure 1. The length L as well as the width W of the heat sink are 0.1143 m (4.5 in), whereas the height H is 0.0381 m. (1.5 in). The conductive base plate, which connects pin-fins, is 0.00635 m (0.25 in) high.

The simulation domain consists of 31 rows of pin-fins in the streamwise direction and 31 rows of pin-fins in the transverse direction. The diameter of the pin-fins is $d = 0.003175$ m (0.125 in). The pitch-to-diameter ratio in the streamwise direction is set to $p_x/d = 1.06$, and in the transverse direction to $p_y/d = 2.12$.

The material properties are also taken from the experimental cases. The heat sink consists of cast aluminum alloy 195 and it is exposed to air cross-flow. The entering flow profile is fully developed due to two rows of honeycomb flow straighteners that were placed in front of the test section. A thermal isolation layer placed between the heater and the aluminum base sets the isothermal conditions at the base bottom.

3.2.   Boundary Conditions

The boundary conditions of the model equations (4), (8), and (12) attempt to represent the experimental situation described previously. As the experimental data were obtained for heating rates $Q = 50$, 125, and 220 W, the numerical simulations were performed for the same heat inputs.

For the momentum transport equation (4), the no-slip boundary conditions are implemented for both walls that are parallel with the flow direction:

$$\bar{u}(0) = 0 \qquad \bar{u}(H) = 0 \tag{13}$$

The preset values of the whole-section pressure drop Δp are summarized in Table 1.

For the fluid-phase energy transport equation (8), the simulation domain inflow and the bottom wall are taken as isothermal,

$$\bar{T}_f(0, z) = T_{\text{in}} \qquad \bar{T}_f(x, 0) = T_g \tag{14}$$

whereas the upper boundary is adiabatic,

$$\frac{\partial \bar{T}_f}{\partial z}(x, H) = 0 \tag{15}$$

The inflow boundary values T_{in} and the bottom wall values T_g are summarized in Tables 2 and 3.

For the solid-phase energy transport equation (12), the bottom wall was prescribed as isothermal, whereas the top wall was assumed to be adiabatic:

$$\bar{T}_s(x, 0) = T_g \qquad \frac{\partial \bar{T}_s}{\partial z}(x, H) = 0 \tag{16}$$

The bottom wall values T_g are summarized in Table 3.

It has to be noted that the assumption of an isothermal bottom wall, Eqs. (14) and (16), differs significantly from the experimental setup, where the pin-fins were connected with a conductive base plate. This approximation can be made, if the height of the base plate is small and its heat conductivity is high enough. As simulations will show, this assumption has a minor effect on the results.

Table 1. Whole-section pressure drop Δp [Pa] at 50, 125, and 220 W

Δp [Pa] at 50 W	5.0	10.0	20.0	40.0	74.72	175.6	266.5	368.6
Δp [Pa] at 125 W	5.0	10.0	20.0	40.0	74.72	179.3	274.0	361.1
Δp [Pa] at 220 W	5.0	10.0	20.0	40.0	74.72	180.6	280.2	361.1

Table 2. Inflow temperature T_{in} [°C] at 50, 125, and 220 W

T_{in} [°C] at 50 W	23.0	23.0	23.0	23.0	23.02	23.02	23.04	22.85
T_{in} [°C] at 125 W	23.0	23.0	23.0	23.0	23.16	23.21	23.05	22.81
T_{in} [°C] at 220 W	23.0	23.0	23.0	23.0	23.07	22.96	22.97	22.90

Table 3. Bottom temperature T_g [°C] at 50, 125, and 220 W

T_g [°C] at 50 W	54.9	43.43	37.2	33.0	30.3	27.9	27.3	26.64
T_g [°C] at 125 W	103.8	74.6	58.8	48.15	41.8	35.73	33.6	32.25
T_g [°C] at 220 W	168.0	114.8	87.0	68.0	56.4	45.2	42.3	40.4

4. SOLUTION METHODS

In spite of the availability of more general numerical methods, we tried to find a semianalytical solution of Eqs. (4), (8), and (12) that can be used as a reference solution of the conjugate heat transfer problems. For that purpose the semianalytical Galerkin approach was used.

4.1. Scaling Procedure

In order to construct the Galerkin solution method, the developed transport equations (4), (8), and (12), as well as the appropriate boundary conditions (13)–(16), need to be transformed into dimensionless form. The dimensionless form of equations enables one to use more general algorithms that are already developed and are publicly accessible.

As all of the equation variables are already averaged over the appropriate V_k, the averaging symbol will be omitted. Furthermore, to distinguish the dimensional from the nondimensional form of equations, the caret symbol $\hat{\ }$ will be used to mark dimensional variables in this section.

Equation (17) presents scaling factors for the spatial coordinates x and z:

$$\hat{x} = \hat{L}x \qquad \hat{z} = \hat{H}z \tag{17}$$

Scaling factors for the kinematic variables are presented in Eq. (18):

$$\hat{u} = \hat{U}u \qquad \hat{p} = \hat{\rho}_f \hat{U}^2 p \qquad \hat{U} = \sqrt{\frac{\Delta \hat{p}}{\hat{\rho}_f}} \tag{18}$$

The scaling relations for fluid and solid temperatures are given in Eq. (19):

$$\hat{T}_g - \hat{T}_f = \left(\hat{T}_g - \hat{T}_{in}\right) T_f \qquad \hat{T}_g - \hat{T}_s = \left(\hat{T}_g - \hat{T}_{in}\right) T_s \tag{19}$$

Applying the scaling laws (17) and (18) to the momentum transport equation (4) yields

$$-\frac{\alpha_f}{\text{Re}_s}\left(\frac{\hat{d}_h^2}{\hat{H}^2}\right)\frac{\partial^2 u}{\partial z^2} + \frac{1}{2}C_l\left(\hat{d}_h \hat{S}\right)u^2 = \frac{\hat{d}_h}{\hat{L}} \tag{20}$$

Finally, the momentum transport equation can be written as

$$-M_2 \frac{\partial^2 u}{\partial z^2} + M_3 u^2 = M_4 \tag{21}$$

where M_2, M_3, and M_4 are constants. Based on the scaling laws, the boundary conditions (13) change to

$$u(0) = 0 \qquad u(1) = 0 \tag{22}$$

When the scaling laws (17)–(19) are introduced to the fluid-phase energy transport equation (8), the equation changes to

$$\alpha_f \text{Pr Re}_s \left(\frac{\hat{d}_h}{\hat{L}}\right) u \frac{\partial T_f}{\partial x} = \alpha_f \left(\frac{\hat{d}_h^2}{\hat{H}^2}\right)\frac{\partial^2 T_f}{\partial z^2} - \text{Nu}_s\left(\hat{d}_h \hat{S}\right)(T_f - T_s) \tag{23}$$

Equation (23) can be further simplified to

$$F_1 u \frac{\partial T_f}{\partial x} = F_4 \frac{\partial^2 T_f}{\partial z^2} - F_5(T_f - T_s) \tag{24}$$

where F_1, F_4, and F_5 are constants. Based on the scaling laws, the boundary conditions (14) and (15) change to

$$T_f(0, z) = 1 \qquad T_f(x, 0) = 0 \qquad \frac{\partial T_f}{\partial z}(x, 1) = 0 \tag{25}$$

As in the previous case, inserting the scaling laws (17)–(19) to the solid-phase energy transport equation (12) gives the following form:

$$0 = \alpha_s \left(\frac{\hat{d}_h^2}{\hat{H}^2} \right) \frac{\partial^2 T_s}{\partial z^2} + \mathrm{Nu}_s \left(\frac{\hat{\lambda}_f}{\hat{\lambda}_s} \right) \left(\hat{d}_h \hat{S} \right) (T_f - T_s) \tag{26}$$

Next, the solid-phase energy transport equation (26) is reduced to

$$0 = S_1 \frac{\partial^2 T_s}{\partial z^2} + S_2(T_f - T_s) \tag{27}$$

where S_1 and S_2 are constants. The solid structure boundary conditions (16) also change to

$$T_s(x, 0) = 0 \qquad \frac{\partial T_s}{\partial z}(x, 1) = 0 \tag{28}$$

4.2. Galerkin Solution Procedure

The momentum transport equation (21) is first linearized to

$$- M_2 \frac{\partial^2 u}{\partial z^2} + Ku = M_4 \tag{29}$$

with $K = M_3 u$ being a constant. The solution of the linearized momentum transport equation (29) is expected to be of the form

$$u \sim \exp(\gamma z) \tag{30}$$

where γ is a constant. Taking into account the boundary conditions given by Eq. (22), the fluid velocity is

$$u = A_1 \exp(\gamma z) + A_2 \exp(-\gamma z) + \frac{M_4}{K} \tag{31}$$

where γ, A_1, and A_2 are constants defined from boundary conditions.

To find the solution to the system of energy transport equations (24) and (27), both equations are combined into the single expression

$$u F_1 \frac{\partial T_s}{\partial x} + F_4 \frac{S_1}{S_2} \frac{\partial^4 T_s}{\partial z^4} - \left(F_5 \frac{S_1}{S_2} + F_4 \right) \frac{\partial^2 T_s}{\partial z^2} - u F_1 \frac{S_1}{S_2} \frac{\partial^3 T_s}{\partial x \partial z^2} = 0 \tag{32}$$

which can be written in a more compact form as

$$D_1 \frac{\partial T_s}{\partial x} + D_2 \frac{\partial^4 T_s}{\partial z^4} - D_3 \frac{\partial^2 T_s}{\partial z^2} - D_4 \frac{\partial^3 T_s}{\partial x \, \partial z^2} = 0 \tag{33}$$

where D_2, D_3 are constants and D_1, D_4 are functions of z.

Next, separation of variables in the following form is used to find the solution of Eq. (33):

$$T_s = X(x)Z(z) \tag{34}$$

with the boundary conditions

$$X(0) = 1 \qquad Z(0) = 0 \qquad \frac{\partial Z}{\partial z}(1) = 0 \tag{35}$$

When Eq. (34) is inserted in Eq. (33), the following differential equation is obtained:

$$D_1 Z X^I + D_2 Z^{IV} X - D_3 Z^{II} X - D_4 Z^{II} X^I = 0 \tag{36}$$

The solution in the z direction of Eq. (36) is anticipated to be a finite set of orthogonal functions,

$$Z = A_n Z_n \qquad Z_n = \sin(\gamma_n z) \qquad \gamma_n = \frac{2n-1}{2}\pi \tag{37}$$

which satisfy the boundary conditions (35). Introducing Eq. (37) into Eq. (36) brings us to

$$D_1 X^I(A_n Z_n) + D_2 X(A_n \gamma_n^4 Z_n) + D_3 X(A_n \gamma_n^2 Z_n) + D_4 X^I(A_n \gamma_n^2 Z_n) = \text{error} \tag{38}$$

and in a more compact form to

$$X^I A_n \big(D_1 + \gamma_n^2 D_4\big) Z_n + X A_n \big(\gamma_n^4 D_2 + \gamma_n^2 D_3\big) Z_n = \text{error} \tag{39}$$
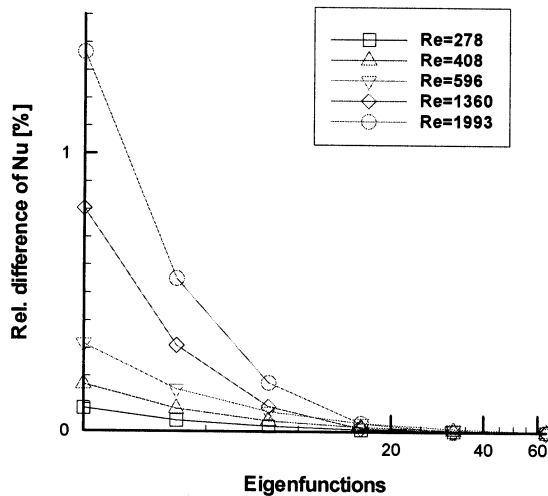
Figure 2. Analysis of results consistency, $Q = 150\,\text{W}$.

As the series is finite, there is a certain discrepancy associated with the expansion. This error is orthogonal to the set of functions used for the expansion and can be reduced with multiplication by Z_m ($m = 1$, N) and further integration from 0 to 1:

$$X^I A_n \int_0^1 \left(D_1 + \gamma_n^2 D_4\right) Z_n Z_m \, dz + X A_n \int_0^1 \left(\gamma_n^4 D_2 + \gamma_n^2 D_3\right) Z_n Z_m \, dz = 0 \qquad (40)$$

In matrix form, Eq. (40) is written as

$$X^I A_n I_{nm} + X A_n J_{nm} = 0 \qquad (41)$$

where I_{nm} and J_{nm} are z-dependent integrals. As the x- and z-dependent parts of Eq. (41) can be separated,

$$\beta = -\frac{X_m^I}{X_m} = \frac{A_n J_{nm}}{A_n I_{nm}} \qquad (42)$$

separate equations are written for the x direction,

$$X_m^I + \beta_m X_m = 0 \qquad (43)$$

and for the z direction,

$$A_n J_{nm} - \beta_m A_n I_{nm} = 0 \qquad (44)$$

The solution of Eq. (43) is obtained by integration:

$$X_m = C \exp(-\beta_m x) \qquad (45)$$

where C and β_m are arbitrary constants. Rearranging Eq. (44), an extended eigenvalue problem can be formed as

$$(J_{nm} - \beta_m I_{nm}) A_n = 0 \qquad (46)$$

The system of Eq. (46) has a nontrivial solution if

$$\mathrm{Det}(J_{nm} - \beta_m I_{nm}) = 0 \qquad (47)$$

From this condition the system eigenvalues β_m are determined. Furthermore, each eigenvalue β_m corresponds to a specific m vector of A_n.

Using the solutions of Eq. (43) and the matrix system (47), one can construct the solid structure temperature field:

$$T_s = C_i X_i A_{in} Z_n \qquad (48)$$

Reintroducing Eq. (27), the fluid temperature field is then given by

$$T_f = C_i X_i A_{in} \left(1 + \frac{S_1}{S_2} \gamma_n^2\right) Z_n \qquad (49)$$

The coefficients C_i are found from the initial condition $T_f(0, z) = 1$:

$$C_i A_{in} \left(1 + \frac{S_1}{S_2} \gamma_n^2\right) Z_n = 1 \qquad (50)$$
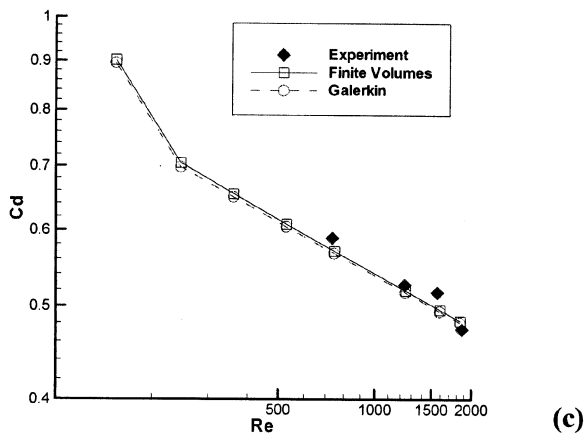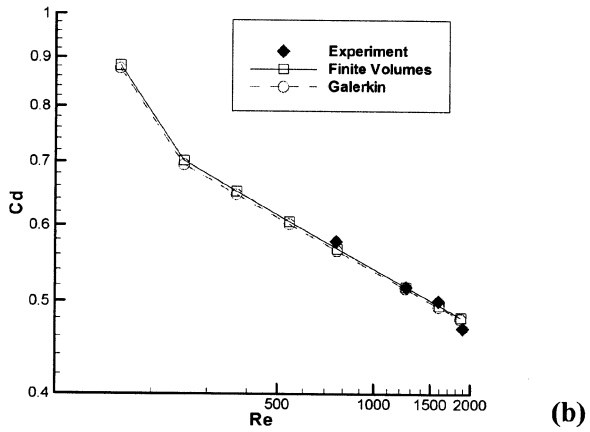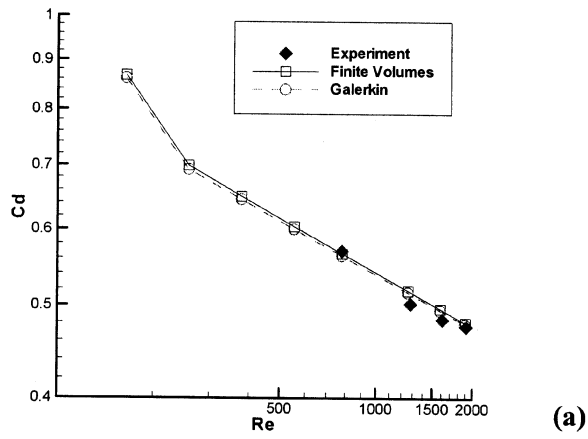
Figure 3. Whole-section drag coefficient C_d, $Q = 50\,\text{W}$ (*a*), $125\,\text{W}$ (*b*), and $220\,\text{W}$ (*c*).
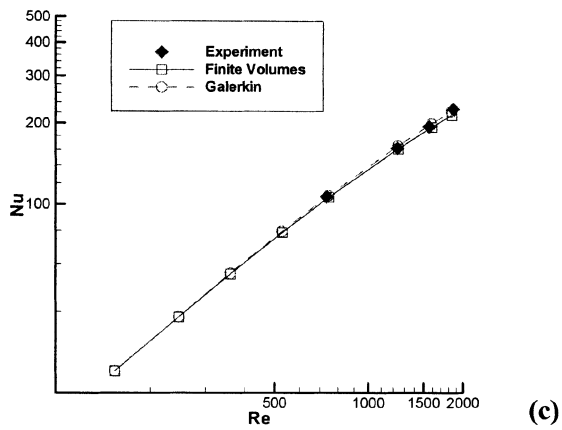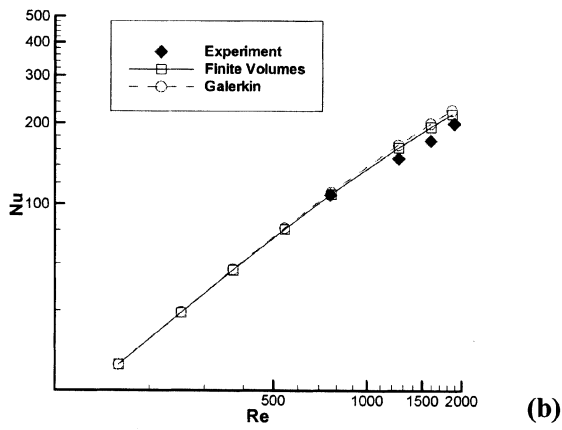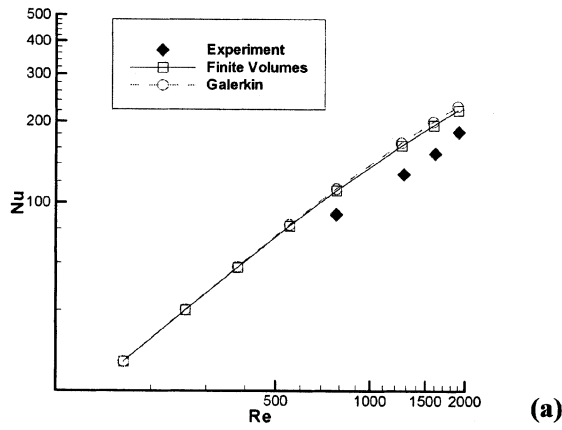
Figure 4. Whole-section Nusselt number Nu, $Q = 50\,\mathrm{W}$ (a), $125\,\mathrm{W}$ (b), and $220\,\mathrm{W}$ (c).
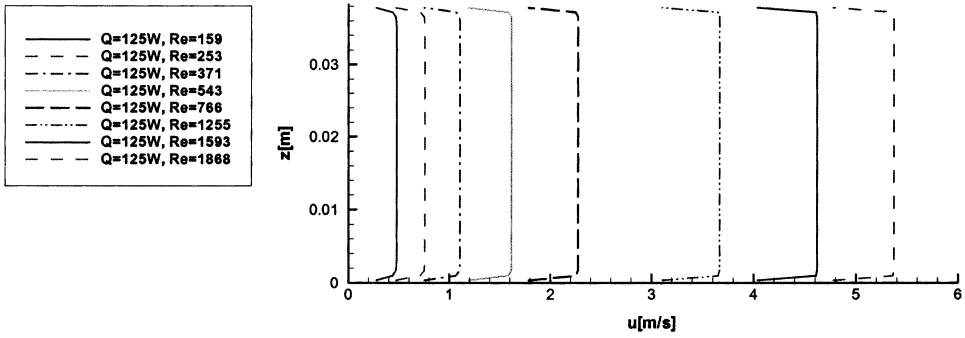
Figure 5. Fluid velocity cross section, $Q = 125\,\text{W}$, GM.

Again, using the same procedure by multiplying Eq. (50) with Z_m ($m = 1$, N) and integrating it from 0 to 1,

$$C_i A_{in}\left(1 + \frac{S_1}{S_2}\gamma_n^2\right)\int\limits_0^1 Z_n Z_m \, dz = \int\limits_0^1 Z_m dz \tag{51}$$

(a)

(b)
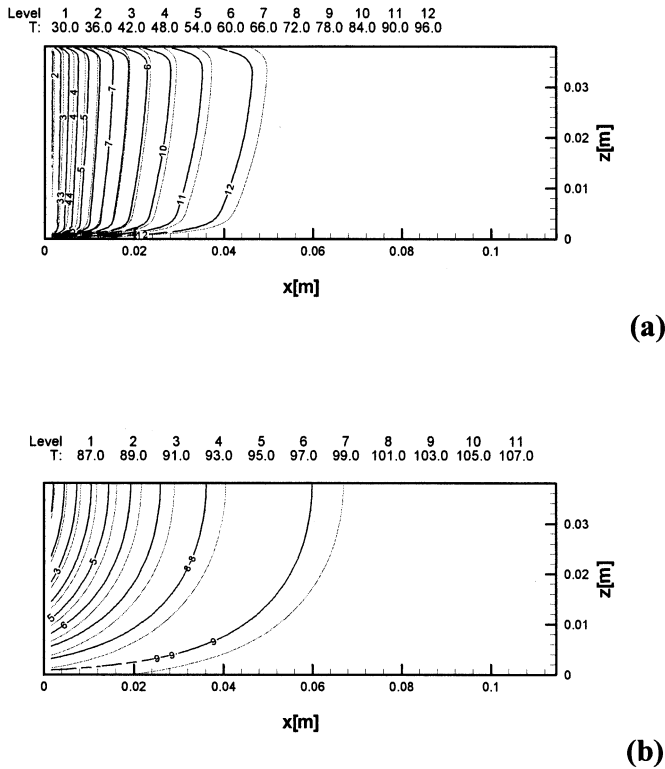
Figure 6. Temperature field in the fluid (*a*) and the solid (*b*); GM (black) and FVM (gray); $\text{Re}_h = 159$, $Q = 125\,\text{W}$.
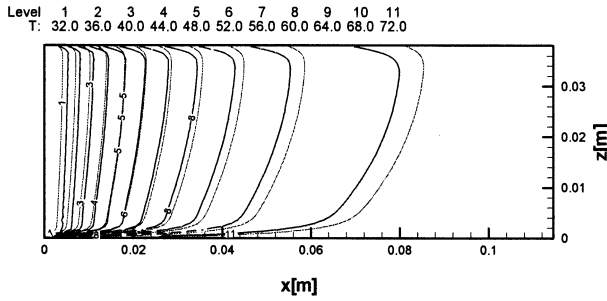
(a)
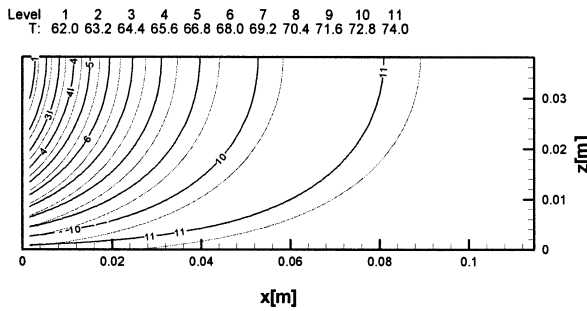
(b)

Figure 7. Temperature field in the fluid (*a*) and the solid (*b*); GM (black) and FVM (gray); $\text{Re}_h = 253$, $Q = 125\,\text{W}$.

the orthogonality condition reduces Eq. (51) to

$$C_i A_{im} \left(1 + \frac{S_1}{S_2} \gamma_m^2 \right) I_m = J_m \tag{52}$$

where I_m and J_m are analytically calculated integrals. Writing Eq. (52) in a matrix form,

$$A_{im} C_i = \frac{J_m}{\left[1 + S_1/S_2 \gamma_m^2 \right] I_m} \tag{53}$$

the unknown coefficients C_i are calculated with inversion of the matrix system (53).

5. RESULTS

Simulations of the heat sink thermal behavior were performed for the pressure drops Δp and the boundary temperatures T_{in} and T_g, which are summarized in Tables 1, 2, and 3. Calculations were performed at heating powers $Q = 50$, 125, and 220 W to match the experimental data obtained by Rizzi et al. [21].

(a)

(b)
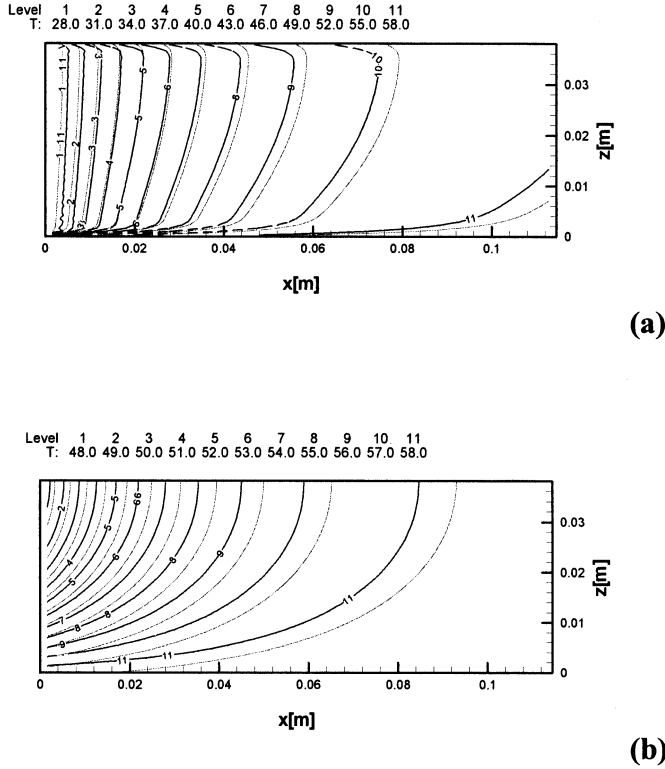
Figure 8. Temperature field in the fluid (*a*) and the solid (*b*); GM (black) and FVM (gray); $\mathrm{Re}_h = 371$, $Q = 125\,\mathrm{W}$.

5.1. Comparison of Whole-Section Values

The imposed pressure drop Δp causes air flow across the heated solid structure. As the structure is cooled, a steady temperature field is formed in the air flow as well as in the thermally conductive aluminum. Based on the calculated velocity and temperature fields, the whole-section drag coefficient,

$$C_d = \frac{2\Delta p A_\perp}{\rho_f [u]^2 A_o} \tag{54}$$

and the whole-section Nusselt number,

$$\mathrm{Nu} = \frac{Q d_h}{(T_g - T_{\mathrm{in}}) A_g \lambda_f} \tag{55}$$

were estimated as functions of Reynolds number Re_h. In Eq. (54), $[u]$ marks average streamwise velocity in the whole simulation domain.

The whole-section values of the drag coefficient C_d and Nusselt number Nu calculated with the Galerkin method (GM) are compared with the results of the finite-volume method (FVM) (Horvat [17]) and with the experimental data taken by Rizzi et al. [21]. As the experimental methods cannot give a detailed picture of
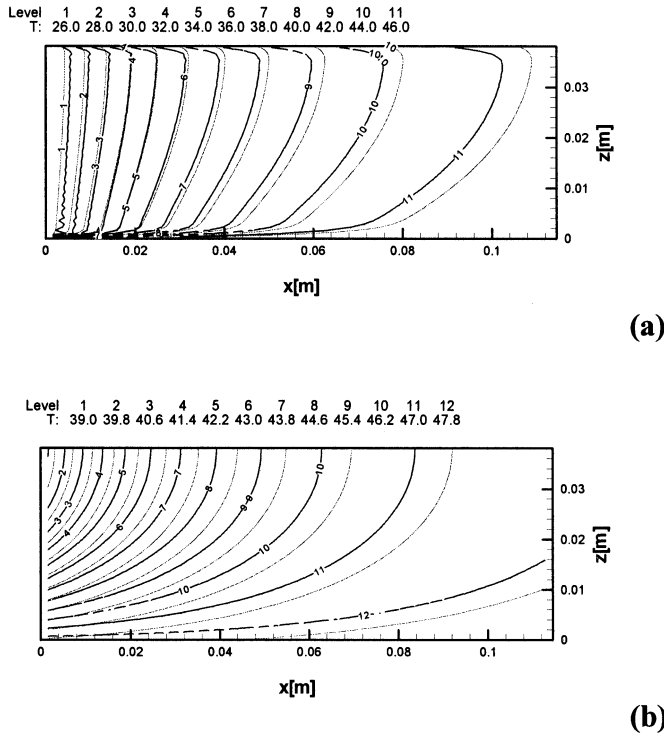
(a)

(b)

Figure 9. Temperature field in the fluid (*a*) and the solid (*b*); GM (black) and FVM (gray); $Re_h = 543$, $Q = 125\,W$.

velocity and temperature fields, the comparisons of these whole-section values serve as the verification of the constructed physical model and validate the developed numerical code.

The consistency analysis was also performed. For this purpose the simulations were done with $N = 2, 4, 8, 16, 32$, and 64 eigenfunctions (37), and the whole-section Nusselt number Nu was calculated for different Reynolds numbers. Figure 2 presents only a part of the results, in order to prove consistency of the developed procedure. It is evident that for Reynolds number $Re_h = 1993$, the whole-section Nusselt number Nu calculated with only 2 eigenfunctions differs for 1.4% from the one calculated with 64 eigenfunctions. As the number of eigenfunctions used increases, the difference decreases even further.

Figures 3 show the whole-section drag coefficient C_d [Eq. (54)] as a function of Reynolds number Re_h at thermal powers $Q = 50, 125$, and $220\,W$. The results calculated with the GM (marked with Galerkin) are close to the results obtained by the FVM (marked with finite volumes) as well as to the experimental data (marked with Experiment). Slight discrepancy from the experimental data at higher Reynolds number is due to transition to turbulence, which is evident in the experimental results, but is not captured by the model. For thermal power $Q = 125\,W$, Figure 3*b* shows good agreement between the GM results, the FVM results, and the experimental data. The difference is visible only at the last experimental point

(a)

(b)
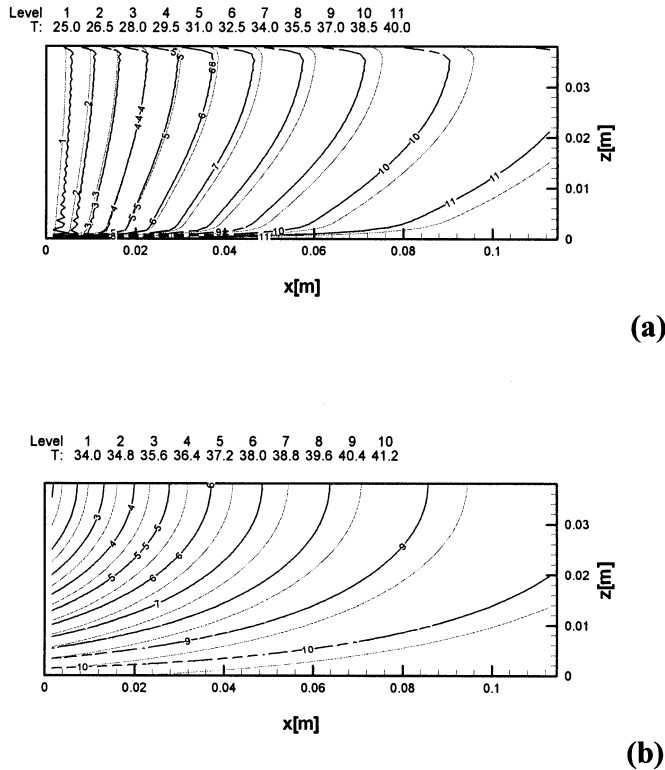
Figure 10. Temperature field in the fluid (*a*) and the solid (*b*); GM (black) and FVM (gray); $Re_h = 766$, $Q = 125\,W$.

($Re_h = 1912$), where the transition effects are already present. Although Figure 3*c* still shows good agreement between both models and experimental data, larger discrepancies are already visible. Namely, at thermal power $Q = 220\,W$ the air flow through the heat sink is strongly influenced by thermal stratification, due to intensive heating at the bottom. The resulting buoyancy effects cause model deficiencies as well as problems with the representation of collected experimental data.

Figures 4 show the whole-section Nusselt number Nu [Eq. (55)], as a function of Reynolds number Re_h at thermal powers $Q = 50$, 125, and 220 W. The Nusselt number distributions at thermal power $Q = 50\,W$ are presented in Figure 4*a*. They show a larger difference between the GM and FVM results on one side and the experimental data on the other. The difference of approximately 10% is steady throughout the whole range of tested Reynolds numbers Re_h, which is believed to be a consequence of systematic modeling or experimental error. Figure 4*b*, which shows the whole-section Nusselt number Nu at thermal power $Q = 125\,W$, displays only a minor difference of approximately 5% as the Reynolds number increases from $Re_h = 762$ to $Re_h = 1,893$. At thermal power $Q = 220\,W$ (Figure 4*c*), the difference between calculated values and experimental data becomes negligible.
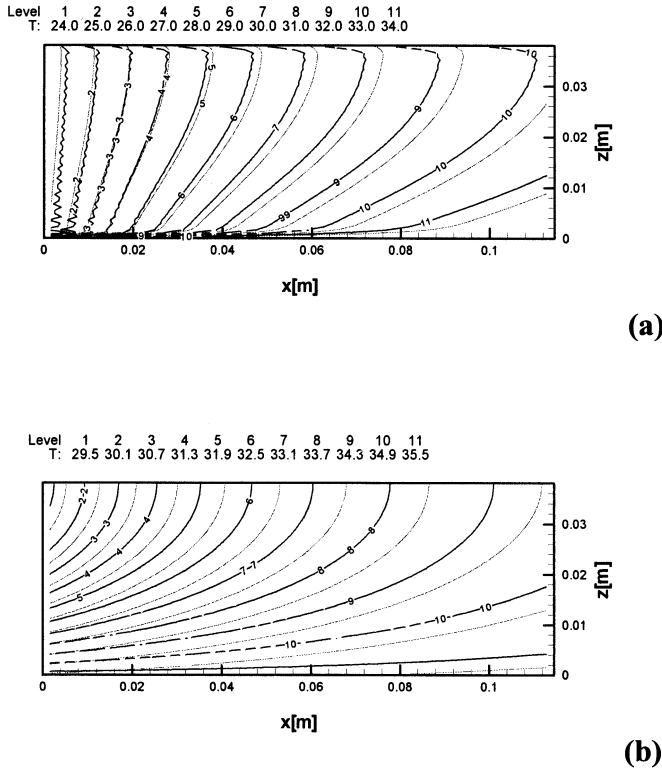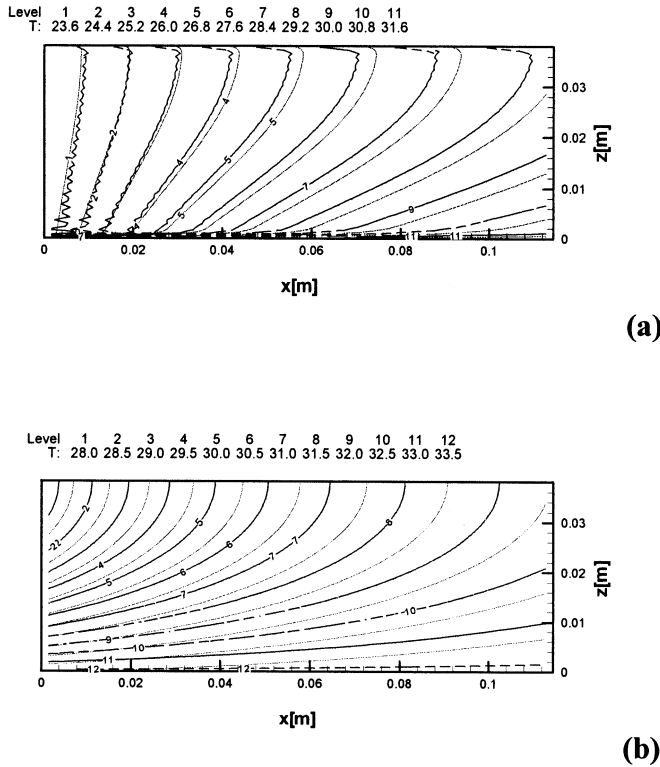
(a)

(b)

Figure 11. Temperature field in the fluid (*a*) and the solid (*b*); GM (black) and FVM (gray); $Re_h = 1255$, $Q = 125\,\text{W}$.

5.2. Temperature Distribution in Heat Sink

The detailed temperature fields at different Reynolds number Re_h give an insight into the heat transfer conditions in the studied heat sink. For calculations performed by the GM, 34×140 mesh points in the *x* and *z* directions were used to simulate heat transfer processes in the fluid and solid phases. As the accuracy of the semianalytical GM is essentially connected with the number of orthogonal functions used for expansion, Eq. (37), 45 basis functions are used in all cases presented. Based on the consistency analysis performed, we are convinced that the maximum associated error can reach up to 1% for the highest tested Reynolds number Re_h.

It should be also noted that although different heating power Q is used at the bottom, there exists a similarity in forced–convection heat removal from the heat sink structure. Namely, higher heat input causes higher absolute temperature levels, whereas the form of isotherms changes only slightly, due to modification in air material properties. Therefore, this article presents the velocity profiles and temperature fields only for thermal power $Q = 125\,\text{W}$.

Figure 5 gives velocity profiles of the air flow at different Reynolds numbers Re_h. The core of the simulation domain has a flat velocity profile due to drag associated with the submerged pin-fins. As the drag is smaller at lower Reynolds numbers Re_h, the boundary layers close to the bottom and the top are much better

Level   1   2   3   4   5   6   7   8   9   10   11
T: 23.6 24.4 25.2 26.0 26.8 27.6 28.4 29.2 30.0 30.8 31.6

(a)

Level   1   2   3   4   5   6   7   8   9   10   11   12
T: 28.0 28.5 29.0 29.5 30.0 30.5 31.0 31.5 32.0 32.5 33.0 33.5

(b)

Figure 12. Temperature field in the fluid (*a*) and the solid (*b*); GM (black) and FVM (gray); $Re_h = 1593$, $Q = 125\,W$.

resolved. Nevertheless, the GM cannot resolve the boundary layer correctly. Compared to the FVM it overpredicts the boundary-layer thickness and therefore reduces the wall friction (Horvat [17]).

Figures 6–13 show the temperature field cross sections at different Reynolds numbers Re_h. The temperatures are in degrees Celsius. Figures marked (*a*) present the temperature field in fluid flow, whereas figures marked (*b*) reveal the temperature field in the solid structure; black lines mark isotherms calculated with the GM, whereas gray lines mark isotherms calculated with the FVM. Comparisons show that the form of isotherms as well as the absolute temperatures are close together. Larger differences occur close to the bottom due to different thermal boundary conditions.

It is evident that the lowest temperature in the air flow is at the beginning of the heat sink; this is on the left side. Temperature raises as the air passes through the heat-exchanging structure. Therefore, the highest temperatures are expected at the exit; this is on the right side. The temperature field in the solid structure is more vertically stratified as the heat enters the structure from the bottom. As a consequence, the lowest temperature in the solid phase is in the upper left corner and the highest at the bottom.

(a)

(b)
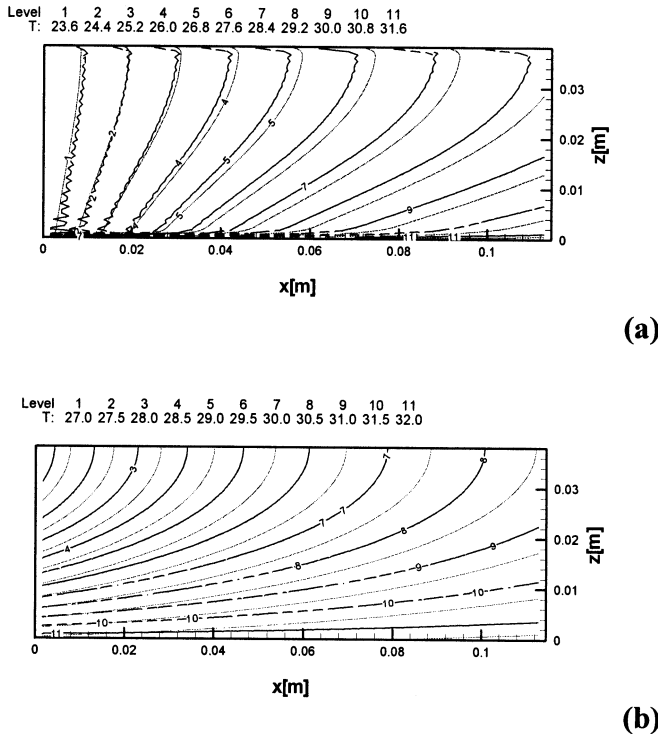
Figure 13. Temperature field in the fluid (*a*) and the solid (*b*); GM (black) and FVM (gray); $Re_h = 1862$, $Q = 125\,W$.

The heat flux is a vector perpendicular to the isotherms and therefore a qualitative picture of heat flow can be extracted from the calculated temperature fields. It can be seen from Figure 8 that most of the heat is transferred from the solid to fluid in the first half of the test section. The highest heat fluxes appear in the lower left corner, where the temperature gradients are the largest. Figures 6–9 reveal that at low Reynolds numbers, the temperature field is not fully developed. This means that the air which enters the test section is quickly heated due to its low velocity and leaves the heat sink at the temperature of the solid phase, unable to receive additional heat from the source. With increasing Reynolds number Re_h, the state of thermal saturation diminishes (Figure 10).

The coolant flow lowers the temperature of the heat-conducting structure unequally. This directly changes the form of isotherms. The effect is not so evident at low Reynolds numbers (Figures 6–8). On the contrary, when the Reynolds number Re_h increases (Figures 9–11), the isotherms become tilted, showing the increasing vertical thermal stratification of the coolant flow.

Figures 10–13 reveal that at current Reynolds numbers the GM already exhibits oscillations on the test section inflow. The oscillations originate from the thermal boundary conditions [Eq. (25)], which form a step function. Such a function is not analytic, therefore the approximation with a series of trigonometric functions

produces oscillations. As the GM still predicts the temperature field with the same accuracy as the FVM in the first half of the simulation domain, the increasing Reynolds number Re_h causes differences between both solutions toward the end of the test section. Nevertheless, the differences for the tested range of Reynolds numbers Re_h were not higher than 5% of the whole-section temperature increase $T_g - T_{in}$.

6. CONCLUSIONS

The article represents a contribution to conjugate heat transfer modeling. In this work the volume averaging technique (VAT) was tested and applied to the simulation of air flow through an aluminum (Al) chip heat sink. The constructed computational algorithm enables prediction of cooling capabilities for the selected geometry. Using the VAT, the computational algorithm is fast-running, but still able to present a detailed picture of temperature fields in air flow as well as in the solid structure of the heat sink.

In the frame of the work performed, the VAT basic rules were used to develop a specific form of the porous media flow model. As the flow variables were averaged over the representative elementary volume (REV), local momentum and thermal interactions between phases had to be replaced with additional models. To close the system of transport equations, reliable data for interphase transfer coefficients were found in Launder and Massey [18], Žukauskas and Ulinskas [20], and Kays and London [19].

The geometry of the simulation domain and the boundary conditions followed the geometry of the experimental test section used in the Morrin-Martinelli-Gier Memorial Heat Transfer Laboratory at the University of California, Los Angeles. The calculations were performed at three different heating powers, $Q = 50$, 125, and 220 W, and eight different pressure drops Δp. The imposed pressure drop achieves coolant flow of Reynolds number Re_h from 159 to 1,862. The semianalytical Galerkin method (GM) was developed for solving the equations. Although the GM is a well-established technique, it has not been used for conjugate heat transfer problems in heat exchanger geometries.

The calculated whole-section drag coefficient C_d and Nusselt number Nu were compared with FVM results and with the experimental data of Rizzi et al. [21] to verify the computational model. The comparison shows good agreement between GM and FVM results. The experimental data exhibit up to 10% difference through the whole computational range of Reynolds numbers Re_h, which is believed to be a consequence of systematic modeling or experimental error.

The detailed temperature fields in the coolant flow as well as in the heat-conducting structure were also calculated and compared with FVM results. The calculated temperature fields in the fluid and the solid reveal up to 5% discrepancy between the two methods, although different thermal boundary conditions at the bottom were used.

The present results demonstrate that the selected Galerkin approach is capable of performing heat exchanger calculations where the thermal conductivity of the solid structure has to be taken into account.

REFERENCES

1. K. A. Antonopoulos, Prediction of Flow and Heat Transfer in Rod Bundles: Results, Ph.D. thesis, Mechanical Engineering Department, Imperial College, London, UK, 1979.
2. H. R. Barsamian and Y. A. Hassan, Large Eddy Simulation of Turbulent Crossflow in Tube Bundles, *Nuclear Eng. Design J.*, vol. 172, pp. 103–122, 1997.
3. A. Horvat and I. Catton, Development of an Integral Computer Code for Simulation of Heat Exchangers, *Proc. 8th Regional Meeting, Nuclear Energy in Central Europe*, Portorož, Slovenia, no. 213, 2001.
4. A. Horvat, M. Rizzi, and I. Catton, Numerical Investigation of Chip Cooling Using Volume Averaging Technique (VAT), in B. Sunden and C. A. Brebbia (eds.), *Advanced Computational Methods in Heat Transfer VII*, pp. 373–382, WIT Press, Southampton, UK, 2002.
5. I. Catton, Convection in a Closed Rectangular Region: The Onset of Motion, *Trans. ASME*, Feb., pp. 186–188, 1970.
6. I. Catton, Effect of Wall Conduction on the Stability of a Fluid in a Rectangular Region Heated from Below, *Trans. ASME*, Nov., pp. 446–452, 1972.
7. J. M. McDonough and I. Catton, A Mixed Finite Difference-Galerkin Procedure for 2D Convection in a Square Box, *Int. J. Heat Mass Transfer*, vol 25, pp. 1137–1146, 1982.
8. L. A. Howle, A Comparison of the Reduced Galerkin and Pseudo-Spectral Methods for Simulation of Steady Rayleigh-Bénard Convection, *Int. J. Heat Mass Transfer*, vol. 39, no. 12, pp. 2401–2407, 1996.
9. T. B. Anderson and R. Jackson, A Fluid Mechanical Description of Fluidized Beds, *Int. Eng. Chem. Fund.*, 6, pp. 527–538, 1967.
10. J. C. Slattery, Flow of Viscoelastic Fluids through Porous Media, *AIChE J.*, vol 13, pp. 1066–1071, 1967.
11. C. M. Marle, Ecoulements monophasiques en milineu poreux, *Rev. Inst. Francais du Petrole*, vol. 22, pp. 1471–1509, 1967.
12. S. Whitaker, Diffusion and Dispersion in Porous Media, *AIChE J.*, vol. 13, pp. 420–427, 1967.
13. P. P. Zolotarev and L. V. Redushkevich, The Equations for Dynamic Sorption in an Undeformed Porous Medium, *Dok. Phys. Chem.*, vol. 182, pp. 643–646, 1968.
14. F. A. L. Dullien, *Porous Media Fluid Transport and Pore Structure*, Academic Press, New York, 1979.
15. L. L. Kheifets and A. V. Neimark, *Multiphase Processes in Porous Media*, Nadra, Moscow, 1982.
16. P. M. Adler, *Porous Media: Geometry and Transport*, Butterworth-Heinemann, Stoneham, MA, 1992.
17. A. Horvat, Calculation of Conjugate Heat Transfer in a Heat Sink Using Volume Averaging Technique (VAT), M.Sc. thesis, University of California, Los Angeles, 2002.
18. B. E. Launder and T. H. Massey, The Numerical Prediction of Viscous Flow and Heat Transfer in Tube Banks, *J. Heat Transfer*, vol. 100, pp. 565–571, 1978.
19. W. S. Kays and A. L. London, *Compact Heat Exchangers*, 3d ed., Krieger, Malabar, FL, pp. 152–155, 1998.
20. A. Žukauskas and A. Ulinskas, Efficiency Parameters for Heat Transfer in Tube Banks, *J. Heat Transfer Eng.*, vol. 5, no. 1, pp. 19–25, 1985.
21. M. Rizzi, M. Canino, K. Hu, S. Jones, V. Travkin, and I. Catton, Experimental Investigation of Pin Fin Heat Sink Effectiveness, *Proc. 35th Natl. Heat Transfer Conf.*, Anaheim, CA, 2001.